Research Square

Preprints are preliminary reports that have not undergone peer review.
They should not be considered conclusive, used to inform clinical practice,
or referenced by the media as validated information.

Green Synthesis and Characterization of Magnetite Nanoparticles Using Ocimum gratissimum Leaf Extract for Enhanced Adsorption of Cefuroxime in Water

Shaaban Sallau

sallaushaaban@gmail.com

Air Force Institute of Technology Kaduna

Joy Yohana Ishaya

Air Force Institute of Technology Kaduna

Amina Junaid

Air Force Institute of Technology Kaduna

Research Article

Keywords: green synthesis, magnetite nanoparticles, Ocimum gratissimum, cefuroxime, adsorption isotherms

Posted Date: November 6th, 2026

DOI: https://doi.org/10.21203/rs.3.rs-11265547/v1

License: This work is licensed under a Creative Commons Attribution 4.0 International License.
Read Full License

Additional Declarations: No competing interests reported.

Green Synthesis and Characterization of Magnetite Nanoparticles Using *Ocimum gratissimum* Leaf Extract for Enhanced Adsorption of Cefuroxime in Water

Sha'ban Sallau[1*], Joy Yohana Ishaya[1] and Amina Junaid[1]

[1]Department of Chemistry, Faculty of Science, Air Force Institute of Technology, P.M.B. 2104, Kaduna State, Nigeria

Corresponding Author: sallaushaaban@gmail.com, Orcid: 0000-0003-3931-3269, Phone no.: +2347065468626

ABSTRACT: Pharmaceutical contaminants, such as cefuroxime, a widely used second-generation cephalosporin, are frequently detected in wastewater due to incomplete removal during conventional treatment, posing risks to aquatic ecosystems and contributing to antimicrobial resistance. This study was carried out to green-synthesize and characterize magnetite (Fe_3O_4) nanoparticles using the aqueous leaf extract of *Ocimum gratissimum* (scent leaf) via co-precipitation, and to evaluate their efficiency in adsorbing cefuroxime from aqueous solution. The nanoparticles were synthesized using iron (III) chloride and iron (II) sulfate precursors in the presence of the leaf extract, which served as a reducing and capping agent, and were characterized using UV-vis spectrophotometry, FTIR spectroscopy, XRD, and SEM-EDX. UV-vis analysis confirmed nanoparticle formation with a surface plasmon resonance peak at 265 nm, while FTIR identified phytochemical functional groups and an Fe−O stretching band at 713 $cm^{-1,}$ confirming the magnetite phase. XRD identified magnetite as the dominant crystalline phase (55.6% by weight) alongside minor hematite, quartz, and clinochlore, consistent with a poorly crystalline, uncalcined green-synthesis product, and SEM revealed irregular, densely packed agglomerates. Batch adsorption studies showed that cefuroxime removal was favoured under acidic conditions, with pH 2 selected as optimum, and equilibrium attained within 120 min. The adsorption kinetics followed the pseudo-second-order model ($R^2 = 0.999$), while equilibrium data fitted the Langmuir isotherm ($R^2 = 0.996$) better than the Freundlich isotherm ($R^2 = 0.972$), indicating monolayer adsorption with a maximum capacity of 62.5 mg/g. An adsorbent dosage of 25 mg gave the highest removal efficiency (29.4%), and thermodynamic analysis revealed the adsorption process to be spontaneous, endothermic ($\Delta H° = +7.8$ kJ/mol), and accompanied by increased randomness at the solid−liquid interface ($\Delta S° = +28.2$ J/mol·K). These findings indicate the feasibility of *Ocimum gratissimum* as a low-cost, locally available green reducing agent for synthesizing magnetite nanoparticles with potential for the remediation of pharmaceutical pollutants from water.

KEYWORDS: *green synthesis, magnetite nanoparticles, Ocimum gratissimum, cefuroxime, adsorption isotherms*

INTRODUCTION

Pharmaceutical contaminants in water bodies have become a critical global environmental concern. Antibiotics are particularly problematic because of their persistence and their contribution to the spread of antimicrobial resistance. Cefuroxime, a second-generation cephalosporin, is

frequently detected in wastewater effluents and surface waters as a result of extensive clinical use and incomplete removal during conventional treatment[1–3]. Conventional treatment processes, including coagulation and biological treatment, are generally inadequate for the complete removal of such recalcitrant compounds[4].

Adsorption has attracted considerable attention as a remediation technique because of its simplicity, high efficiency, and cost-effectiveness[1,5], and nanotechnology has further enhanced adsorptive removal through the development of nano-adsorbents offering high surface area and abundant reactive sites. Magnetite nanoparticles (Fe_3O_4 NPs) are especially attractive adsorbents in this respect, combining high surface area with superparamagnetic behaviour that allows straightforward magnetic separation and surface functionalization[6–8], and have been applied for antibiotic removal through both adsorption and degradation pathways[8–10]. However, the conventional chemical synthesis of magnetite nanoparticles typically involves hazardous reagents and substantial energy input. Green synthesis using plant extracts offers an alternative that eliminates toxic chemicals, proceeds under ambient conditions, and can enhance the biocompatibility of the resulting material, with plant phytochemicals serving as natural reducing and capping agents[7,11,12].

Ocimum gratissimum (scent leaf) is a plant widely available in Nigeria with a rich phytochemical composition dominated by phenolics and flavonoids[13–17]. It has previously been used to synthesize cobalt oxide, silver, and selenium nanoparticles, but its application for the green synthesis of magnetite nanoparticles remains unexplored. Formation of nanoparticles by this route is generally understood to proceed through phytochemical−metal complexation, reduction to form nuclei, particle growth, and stabilization through surface capping, with phenolic compounds and flavonoids primarily responsible for reduction and capping[7,11,13]; extract concentration, pH, temperature, reaction time, and iron-salt concentration are known to influence the resulting particle size, morphology, and properties[18–20].

Several recent studies have investigated the removal of cefuroxime by other means: Ren et al.[1] reported pseudo-second-order kinetics and Langmuir-type adsorption (qm = 156.8 mg/g) using biochar derived from antibiotic mycelial residue, with an exothermic, spontaneous thermodynamic profile; Babarinde et al.[5] obtained comparable behaviour (qm = 142.3 mg/g) using Blighia sapida leaf biochar; Sharma et al.[9] reported similar kinetic and isotherm behaviour for ciprofloxacin on biochar−magnetite nanocomposites; and Wronski et al.[2] and Zeghbib et al.[3] demonstrated

electrochemical and photocatalytic cefuroxime removal, respectively. Despite the demonstrated versatility of *Ocimum gratissimum* for nanoparticle synthesis and the established effectiveness of magnetite nanoparticles for antibiotic removal, no study to date has reported the synthesis of magnetite nanoparticles using *Ocimum gratissimum* extract specifically for cefuroxime adsorption. The optimal synthesis conditions, the physicochemical properties of the resulting nanoparticles, and their adsorption behaviour toward cefuroxime therefore remain unestablished.

The present study addresses this gap. It is scientifically motivated by the empirical data it provides on plant-mediated magnetite synthesis and pharmaceutical adsorption, environmentally motivated by its demonstration of an eco-friendly synthesis route free of hazardous chemicals, and economically motivated by its use of a low-cost, locally available Nigerian plant as an alternative to expensive imported adsorbents. Accordingly, this study aimed to synthesize and characterize magnetite nanoparticles using *Ocimum gratissimum* leaf extract and to evaluate their efficiency for the enhanced adsorption of cefuroxime from aqueous solution, through the following objectives: (i) to synthesize Fe_3O_4 nanoparticles via green co-precipitation using *Ocimum gratissimum* leaf extract; (ii) to characterize the synthesized nanoparticles by UV-vis spectrophotometry, FTIR spectroscopy, XRD, and SEM-EDX; (iii) to investigate the effects of pH, contact time, initial concentration, and adsorbent dosage on cefuroxime removal, and to determine the adsorption kinetics using pseudo-first-order and pseudo-second-order models; and (iv) to establish the adsorption isotherms using the Langmuir and Freundlich models and to evaluate the thermodynamic parameters ($\Delta G°$, $\Delta H°$, $\Delta S°$) governing the adsorption mechanism.

RESULTS AND DISCUSSION

Characterization of the Green-Synthesized Fe_3O_4 Nanoparticles. The green-synthesized Fe_3O_4 nanoparticles were characterized by UV-vis spectrophotometry, FTIR spectroscopy, XRD, and SEM-EDX to confirm nanoparticle formation, identify surface functional groups, determine phase composition, and examine morphology, before their evaluation as adsorbents for cefuroxime.

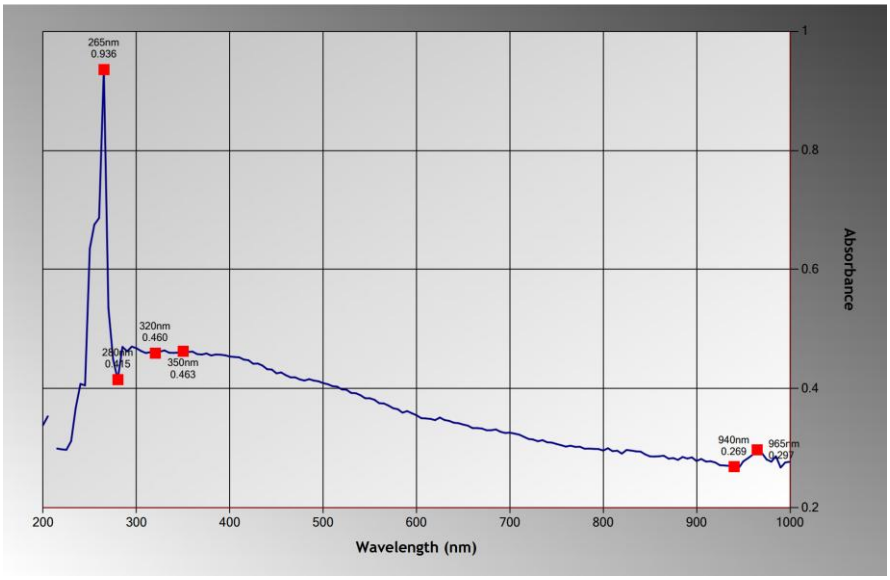


Figure 1. UV−vis spectrum of the green-synthesized Fe_3O_4 nanoparticles over 200−1000 nm.

UV-vis spectrophotometric analysis of the green-synthesized Fe_3O_4 nanoparticles, carried out over 200−1000 nm, showed a characteristic absorption peak at 265 nm (absorbance = 0.936), with additional turning points at 280, 320, 350, 940, and 965 nm and a gradual decrease in absorbance across the 400−800 nm region (Figure 1). This peak, attributable to the surface plasmon resonance characteristic of Fe_3O_4 nanoparticles, confirms nanoparticle formation. The broad nature of the absorption band is typical of green-synthesized nanoparticles and generally reflects the polydisperse nature of the particles and their capping by phytochemicals from the leaf extract, consistent with absorption peaks reported for other green-synthesized magnetite nanoparticles[18,19].

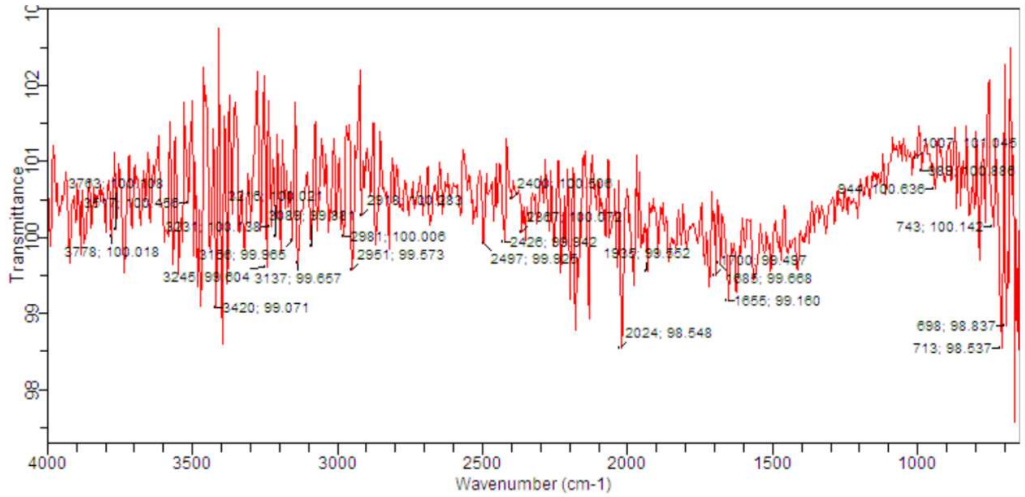


Figure 2. FTIR spectrum of the green-synthesized Fe_3O_4 nanoparticles with phase identification markers.

The FTIR spectrum of the synthesized Fe_3O_4 nanoparticles, recorded over 4000−650 cm^{-1}, showed seven major absorption bands, the wavenumbers and tentative assignments of which are presented in Table 1.

Table 1. FTIR Peak Assignments for the Synthesized Fe_3O_4 Nanoparticles

Wavenumber (cm^{-1})	Assignment	Source
3420	O−H stretching	phenolic compounds, flavonoids
2951	C−H stretching	aliphatic groups
2247	overtone/combination band	aromatic C−H (flavonoids)
2024	overtone/combination band	aromatic ring vibrations
1655	C=O stretching	carboxyl groups, amides (protein capping)
1319	C−O−H bending	alcohols, phenols
713	Fe−O stretching	magnetite (Fe_3O_4)

The broad band at 3420 cm^{-1} indicates hydroxyl groups from phenolics and flavonoids, which are responsible for the reduction of Fe3+ and Fe^{2+} ions during nanoparticle formation, while the band at 713 cm^{-1} is characteristic of Fe−O stretching vibrations in magnetite, confirming successful formation of the Fe_3O_4 phase. The bands at 1655 and 1319 cm^{-1} indicate that phytochemicals from the *Ocimum gratissimum* extract acted as capping agents on the nanoparticle surface, preventing agglomeration and conferring colloidal stability, consistent with previous reports on plant-mediated synthesis of magnetite nanoparticles[13,18,21]. Together, these results confirm both the Fe−O bond signature of magnetite and the presence of a phytochemical capping layer derived from the leaf extract.

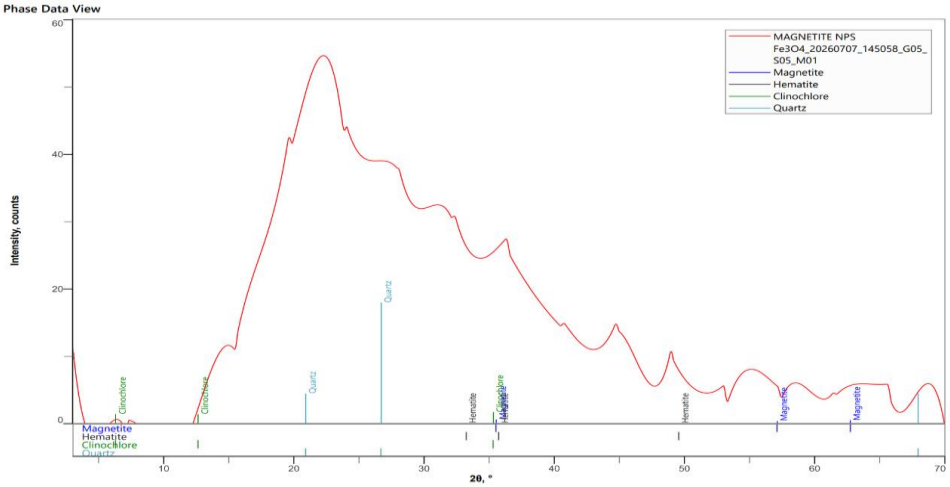


Figure 3. XRD diffractogram of the green-synthesized Fe_3O_4 nanoparticles with phase identification markers.

The crystallographic composition of the synthesized nanoparticles was examined by powder XRD over 2θ = 5−70°. Peak-search analysis identified one resolvable diffraction feature, at 2θ = 22.4(3)°, corresponding to a d-spacing of 3.96(5) Å (Table 2).

Table 2. XRD Peak Parameters of the Synthesized Fe_3O_4 Nanoparticles

2θ (deg)	d-spacing (Å)	height (counts)	fwhm (deg)	apparent size (Å)
22.4(3)	3.96(5)	35(2)	12.9(5)	6.5(2)

Phase search-matching of this feature against the PDF-4 Minerals 2026 database identified overlapping contributions from four candidate phases: magnetite, hematite, clinochlore, and quartz (Table 3).

Table 3. XRD Phase Identification and Quantitative Phase Composition of the Synthesized Fe_3O_4 Nanoparticles

Phase	Formula	space group	figure of merit	weight fraction (%)
Magnetite	Fe_3O_4	Fd-3m:2 (No. 227)	3.450	55.6(15)
Hematite	Fe_2O_3	R-3c:H (No. 167)	3.010	25.5(12)
clinochlore	Al−Fe−Mg silicate (chlorite group)	–	2.222	6.9(4)
quartz	SiO2	P3221 (No. 154)	1.478	12.0(6)

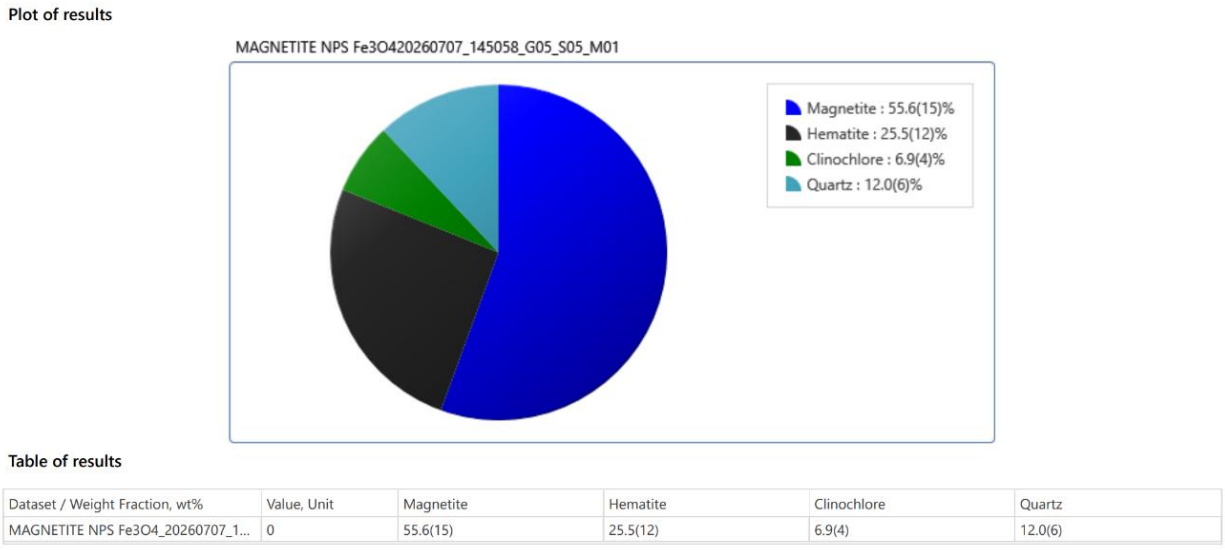
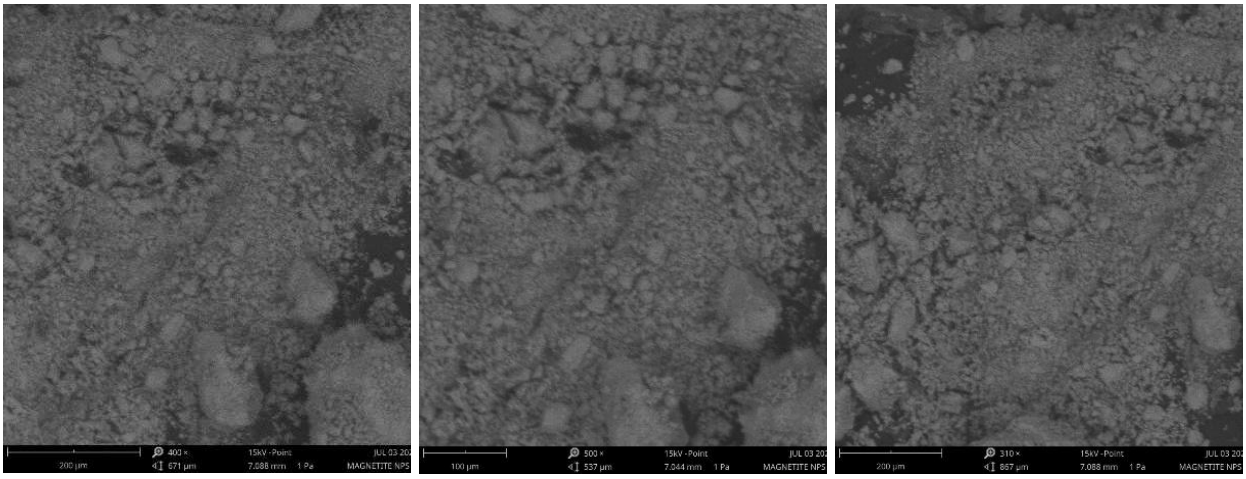


Figure 4. XRD quantitative phase composition (weight fraction) of the synthesized Fe_3O_4 nanoparticles.

Magnetite was identified as the majority crystalline phase (55.6 wt %), confirming that the intended phase was formed. The pattern also revealed hematite (25.5 wt %), a secondary iron oxide phase that commonly arises from partial surface oxidation of magnetite nanoparticles on exposure

to air, particularly given the high surface-to-volume ratio of nanoscale particles, together with minor clinochlore (6.9 wt %) and quartz (12.0 wt %), attributable to trace mineral impurities introduced either from the plant leaf extract or from the precursor salts and glassware used during synthesis; their presence is corroborated by the EDX detection of aluminium, silicon, and magnesium in the same sample. Notably, the diffractogram consisted of a single broad, low-intensity peak (fwhm = 12.9°) rather than the sharp, well-resolved (220), (311), (400), (511), and (440) reflections typically reported for well-crystallized magnetite referenced against JCPDS Card No. 19-0629. The correspondingly small apparent size (6.5 Å) calculated from this broad feature is well below a physically realistic single-domain magnetite crystallite and is better interpreted as an indicator of poor long-range crystalline order than as a literal crystallite dimension. This is consistent with a room-temperature, uncalcined green co-precipitation route, in which capping phytochemicals already evidenced by the FTIR bands discussed above coat the growing nuclei and restrict crystallite growth and ordering. Broad, weakly crystalline XRD signatures of this kind are commonly reported for green-synthesized magnetite nanoparticles obtained without a post-synthesis calcination or annealing step and are generally associated with smaller, more reactive particles offering a comparatively higher surface area, a property favorable for adsorption applications. Overall, the XRD results confirm magnetite as the dominant phase but reveal a poorly crystalline, mixed-phase material rather than a single-phase, highly crystalline product.



(a) 310× *(b) 400×* *(c) 500×*

Figure 5. SEM micrographs of the green-synthesized Fe_3O_4 nanoparticles at (a) 310×, (b) 400×, and (c) 500× magnification.

The surface morphology of the synthesized nanoparticles was examined by SEM at three magnifications (310×, 400×, and 500×; Figure 5a−c) under an accelerating voltage of 15 kV in point/backscatter detection mode, at a chamber pressure of 1 Pa and working distances of 7.044−7.088 mm. The micrographs showed densely packed, irregularly shaped particle agglomerates of varying size distributed across the imaged fields of view (200−867 µm); discrete, well-separated single particles were not resolved at the magnifications used. This morphology is consistent with the poor crystallinity indicated by XRD and with the known tendency of magnetic nanoparticles capped with plant biomolecules to cluster through magnetic dipole−dipole attraction and hydrogen bonding between surface-bound phytochemicals; the magnifications employed were adequate to resolve micron-scale agglomerate morphology but not to resolve individual nanoparticle grains, a limitation of the SEM analysis as performed.

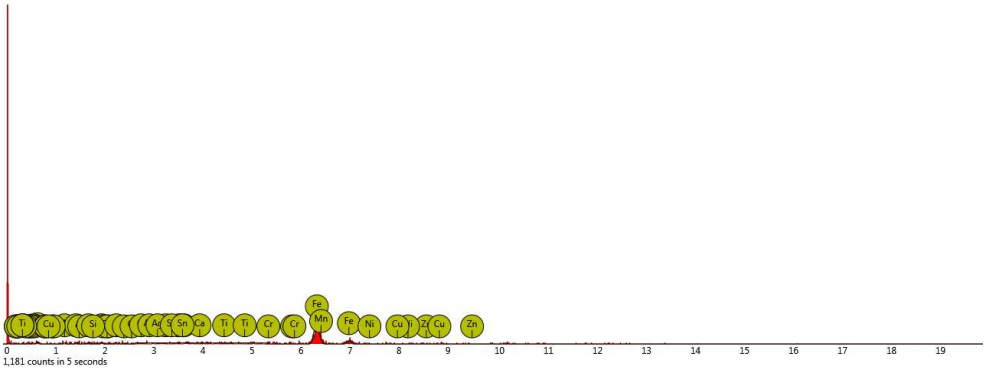


Figure 6. EDX spectrum of the green-synthesized Fe_3O_4 nanoparticles.

Energy-dispersive X-ray (EDX) elemental analysis carried out on the same sample is summarized in Table 4.

Table 4. EDX Elemental Composition of the Synthesized Fe_3O_4 Nanoparticles

element	atomic no.	atomic conc. (%)	weight conc. (%)
iron (Fe)	26	76.91	81.17
zinc (Zn)	30	3.52	4.34
manganese (Mn)	25	2.41	2.50
magnesium (Mg)	12	4.27	1.96
nickel (Ni)	28	1.63	1.81
chromium (Cr)	24	1.56	1.54
phosphorus (P)	15	2.22	1.30
aluminum (Al)	13	2.44	1.24

element	atomic no.	atomic conc. (%)	weight conc. (%)
zirconium (Zr)	40	0.67	1.16
silicon (Si)	14	1.73	0.92
copper (Cu)	29	0.71	0.85
sulfur (S)	16	1.28	0.78
chlorine (Cl)	17	0.65	0.43

EDX confirmed iron as the overwhelmingly dominant element (81.17 wt %), consistent with successful synthesis of an iron oxide-based nanomaterial. The trace elements detected (zinc, manganese, magnesium, nickel, chromium, phosphorus, aluminium, zirconium, silicon, copper, sulphur, and chlorine) are attributable to phytochemical residues and mineral trace impurities, in agreement with the minor clinochlore and quartz phases identified by XRD, while the absence of calcium, potassium, silver, tin, and titanium indicates no major contamination from these common sources. Taken together, the UV-vis, FTIR, XRD, and SEM-EDX results confirm the formation of a magnetite-dominant, phytochemical-capped, nanocrystalline iron oxide material with minor coexisting mineral phases, consistent with a green co-precipitation synthesis route using Ocimum gratissimum leaf extract.

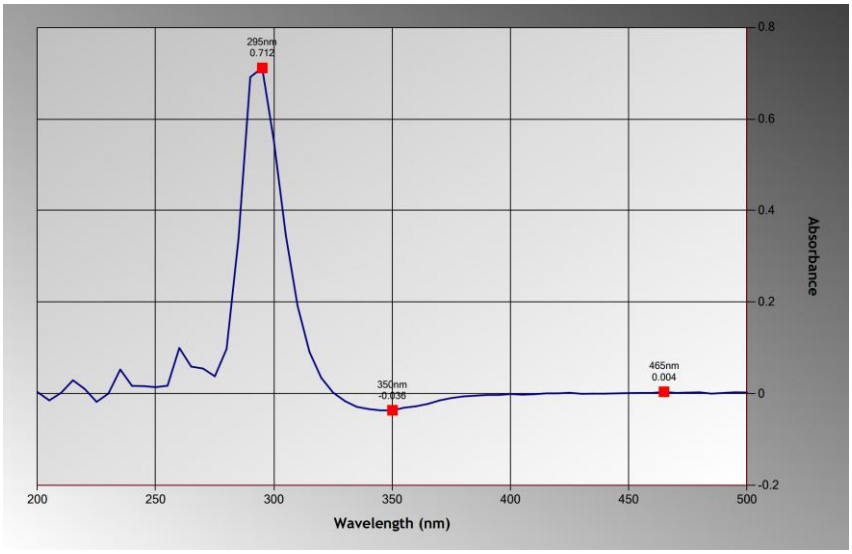


Figure 7. UV−vis spectrum of cefuroxime solution showing λmax at 295 nm.

Calibration Curve and λmax of Cefuroxime. The UV-vis spectrum of cefuroxime solution, recorded over 200−400 nm, showed a wavelength of maximum absorption (λmax) at 295 nm, consistent with the conjugated chromophore of the cephalosporin ring system typical of second-

generation cephalosporins. A calibration curve was constructed at this wavelength using standard solutions of 5−40 mg/L (Figure 8).

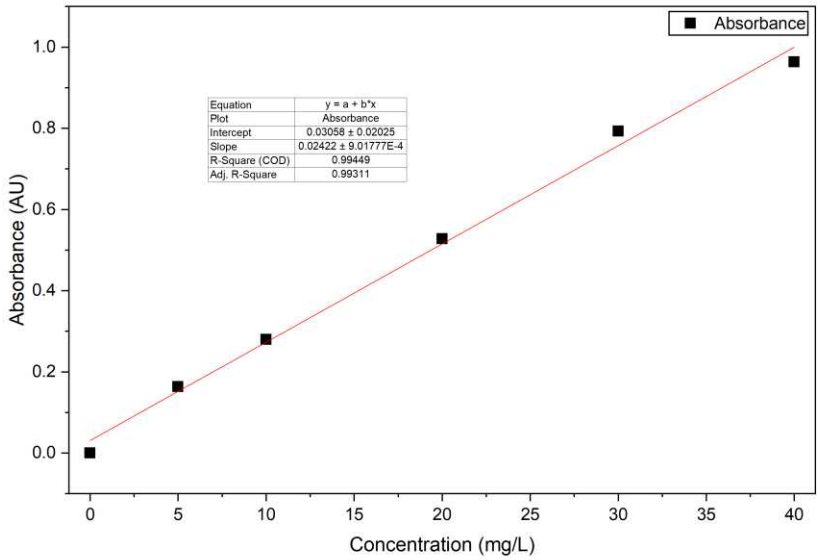


Figure 8. Calibration curve of cefuroxime at 295 nm.

The calibration equation obtained was C = A/0.0242 (R^2 = 0.995), where C is the concentration (mg/L), and A is the absorbance at 295 nm. The high linearity of this calibration confirmed its suitability for reliable quantification of residual cefuroxime concentrations throughout the adsorption experiments, and it was applied to calculate all equilibrium and residual concentrations reported below.

Effect of pH. The effect of pH on cefuroxime adsorption was investigated over pH 2, 4, 6, 8, and 10 (C0 = 49.9 mg/L, adsorbent dosage = 25 mg, volume = 50 mL, contact time = 120 min, temperature = 25 °C); the results are presented in Table 5 and Figure 9.

Table 5. Effect of pH on Cefuroxime Adsorption

pH	Absorbance	Ce (mg/L)	removal (%)	qe (mg/g)
2	0.945	34.4	31.1	31.2
4	1.018	37.0	25.9	25.8
6	1.072	39.0	21.9	21.8
8	1.098	39.9	20.1	20.0
10	1.115	40.5	19.0	18.9

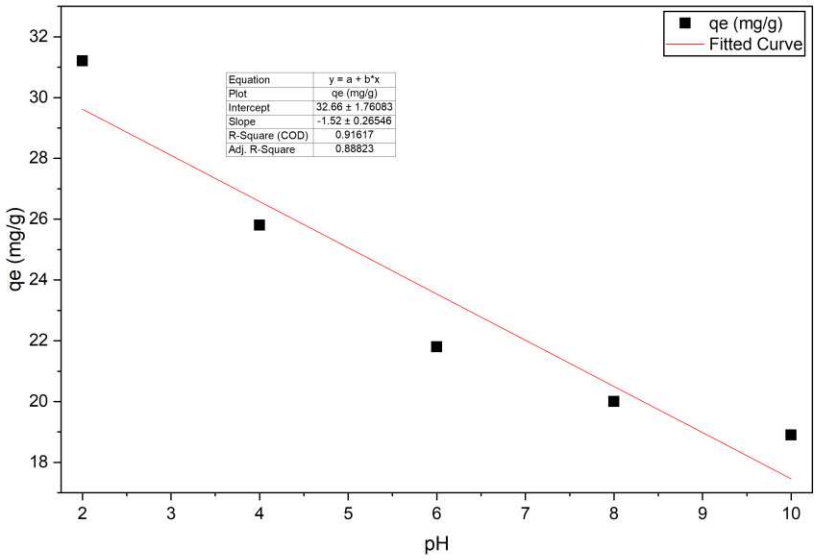


Figure 9. Effect of pH on cefuroxime removal efficiency and adsorption capacity.

Maximum removal (31.1%) was recorded at pH 2, decreasing progressively to a minimum of 19.0% at pH 10; pH 2 was therefore selected as the optimum pH for all subsequent experiments. The decline in removal with increasing pH may be attributed to electrostatic repulsion between the adsorbent surface and the cefuroxime molecule under alkaline conditions, as well as to changes in the ionization state of both the adsorbent surface and the cefuroxime molecule as pH increases.

Effect of Contact Time and Adsorption Kinetics. The effect of contact time was studied at pH 2 (C0 = 50.1 mg/L, adsorbent dosage = 25 mg, volume = 50 mL, temperature = 25 °C) over 5, 15, 30, 60, and 120 min; results are presented in Table 6 and Figure 10.

Table 6. Effect of Contact Time on Cefuroxime Adsorption

time (min)	Absorbance	Ct (mg/L)	removal (%)	qt (mg/g)
5	1.102	40.1	20.0	20.0
15	0.990	36.0	28.1	28.2
30	0.908	33.0	34.1	34.2
60	0.845	30.7	38.7	38.8
120	0.818	29.7	40.7	40.8

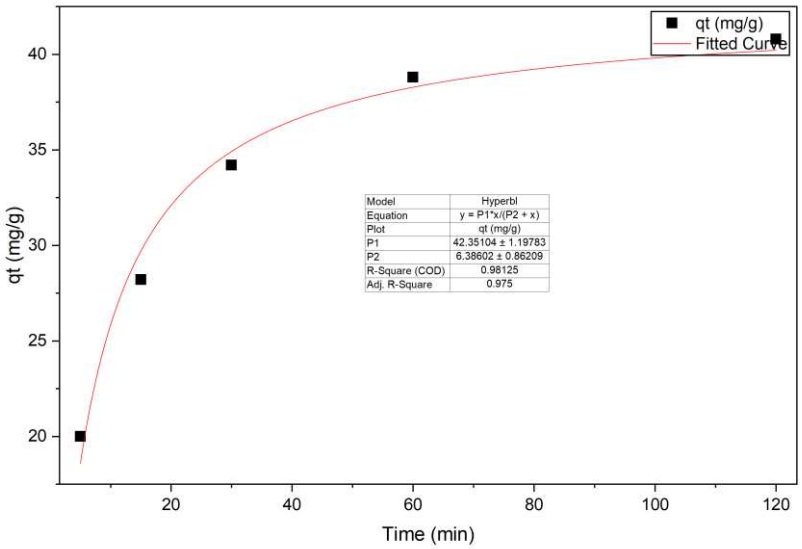
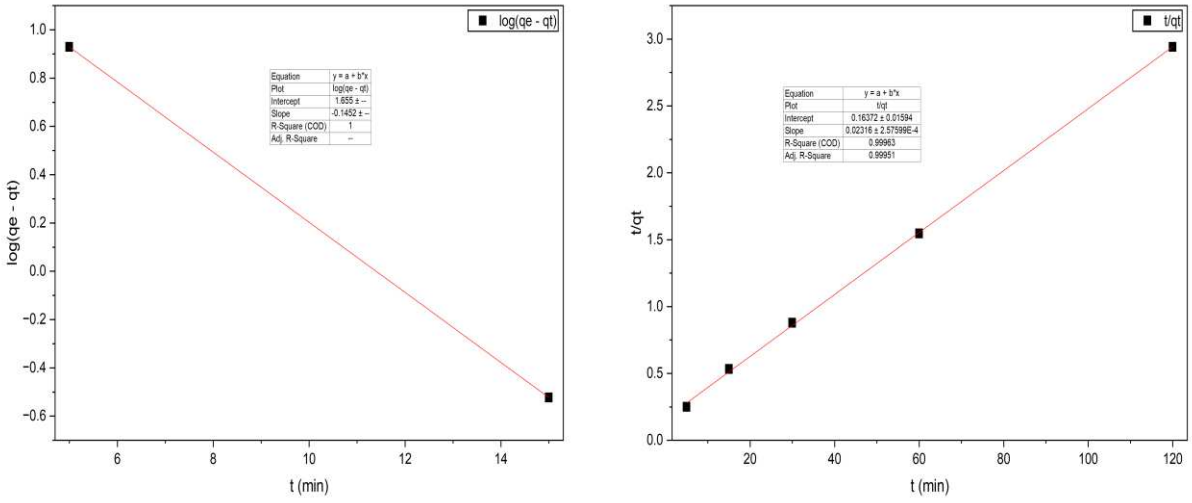


Figure 10. Effect of contact time on cefuroxime adsorption capacity.

Adsorption capacity increased from 20.0 mg/g at 5 min to 40.8 mg/g at 120 min, beyond which no further appreciable increase was recorded; equilibrium was therefore taken as attained at 120 min, with rapid adsorption occurring within the first 30 min followed by a more gradual approach to equilibrium. The contact-time data were fitted to the pseudo-first-order and pseudo-second-order kinetic models (Figure 11); the derived kinetic parameters are summarized in Table 7.



(a) pseudo-first-order *(b) pseudo-second-order*

Figure 11. (a) Pseudo-first-order and (b) pseudo-second-order kinetic plots for cefuroxime adsorption.

Table 7. Kinetic Parameters for Cefuroxime Adsorption

Model	Parameter	Value
pseudo-first-order	k1 (min−1)	0.040
pseudo-first-order	qe (mg/g)	28.5
pseudo-first-order	R^2	1.000
pseudo-second-order	k2 (g/mg·min)	0.0035
pseudo-second-order	qe (mg/g)	42.2
pseudo-second-order	R^2	0.999

Although the pseudo-first-order model returned a nominally higher R^2 (1.000), its fitted equilibrium capacity (qe = 28.5 mg/g) diverges from the experimental value (40.8 mg/g), whereas the pseudo-second-order model, with an equally strong fit (R^2 = 0.999), gives a fitted capacity (42.2 mg/g) close to the experimental value. The pseudo-second-order model is therefore judged to describe the kinetics more reliably, suggesting that chemisorption likely involving valence forces through the sharing or exchange of electrons between the adsorbent surface and the cefuroxime molecule is the rate-limiting step in the adsorption process.

Effect of Initial Concentration and Adsorption Isotherms. The effect of initial cefuroxime concentration was investigated at pH 2 (25 mg adsorbent, 120 min contact time, 25 °C) over 10, 20, 30, 40, and 50 mg/L; results are presented in Table 8 and Figure 12.

Table 8. Effect of Initial Concentration on Cefuroxime Adsorption

C0 (mg/L)	Absorbance	Ce (mg/L)	qe (mg/g)	removal (%)
10.2	0.281	1.8	16.8	82.4
20.0	0.550	4.2	31.6	79.0
30.3	0.833	8.5	43.6	72.0
40.0	1.100	14.2	51.6	64.5
50.1	1.378	20.1	60.0	59.9

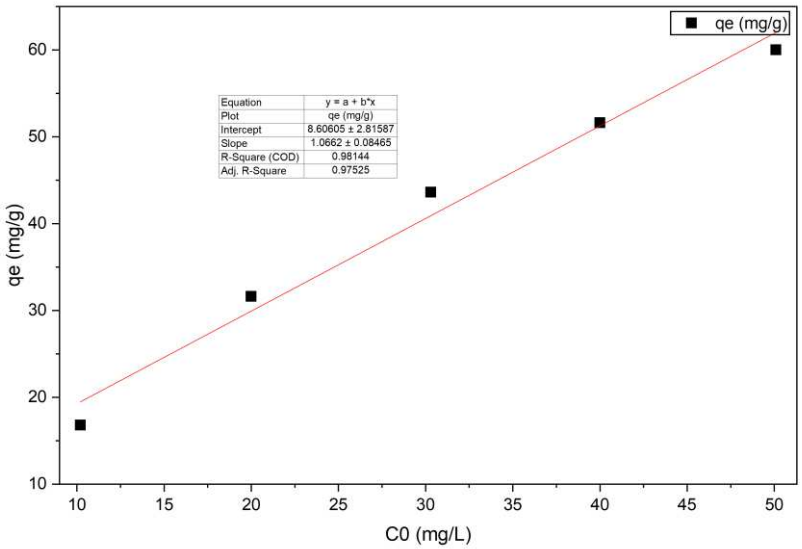
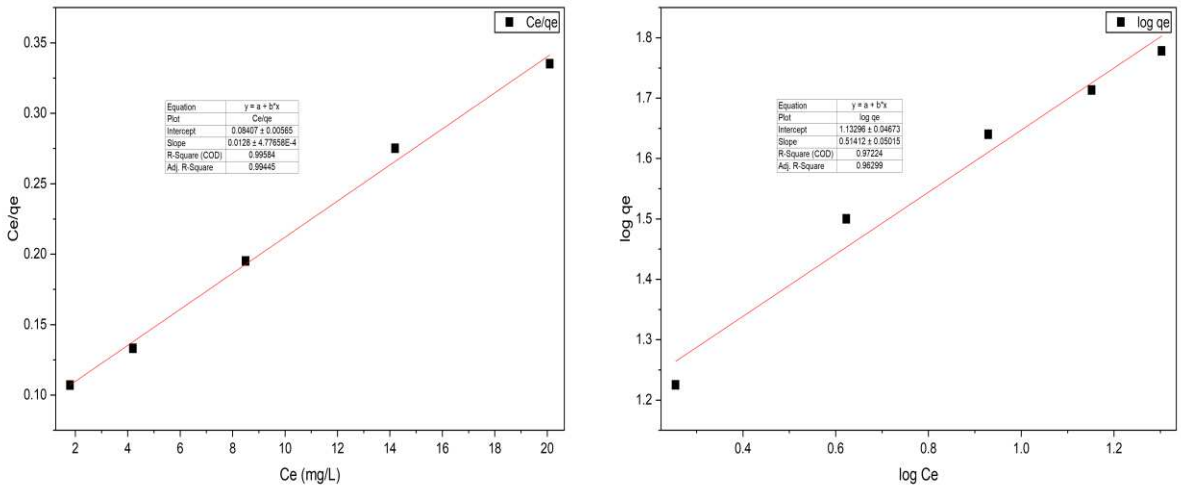


Figure 12. Effect of initial concentration on adsorption capacity.

Adsorption capacity increased with initial concentration, from 16.8 to 60.0 mg/g, reflecting the greater concentration gradient available to drive cefuroxime molecules toward the adsorbent surface at higher initial concentrations, even as percentage removal declined as available active sites became progressively saturated. The equilibrium data were fitted to the Langmuir and Freundlich isotherm models (Figure 13); the derived isotherm parameters are summarized in Table 9.



(a) Langmuir *(b) Freundlich*

Figure 13. (a) Langmuir and (b) Freundlich isotherm plots for cefuroxime adsorption.

Table 9. Isotherm Parameters for Cefuroxime Adsorption

Model	Parameter	Value
Langmuir	qm (mg/g)	62.5
Langmuir	KL (L/mg)	0.078
Langmuir	R^2	0.996
Freundlich	KF (mg/g)	12.5
Freundlich	N	2.65
Freundlich	R^2	0.972

The Langmuir model provided a markedly better fit (R^2 = 0.996) than the Freundlich model (R^2 = 0.972), indicating that adsorption predominantly occurred as a monolayer on a surface of essentially uniform, energetically equivalent sites rather than by multilayer adsorption on a heterogeneous surface. The Langmuir maximum adsorption capacity (qm = 62.5 mg/g) is consistent with the highest experimental qe values obtained in the concentration series. The Langmuir separation factor (RL), calculated at the highest initial concentration tested (C0 = 50.1 mg/L), was 0.20; lying between 0 and 1, this confirms that the adsorption of cefuroxime onto the synthesized Fe_3O_4 nanoparticles is favourable.

Effect of Adsorbent Dosage. The effect of adsorbent dosage was studied at pH 2 (50 mg/L cefuroxime, 120 min contact time, 25 °C) over 10, 25, 50, and 100 mg; results are presented in Table 10 and Figure 14.

Table 10. Effect of Adsorbent Dosage on Cefuroxime Adsorption

dosage (mg)	Absorbance	Ce (mg/L)	removal (%)	qe (mg/g)
10	0.983	35.7	28.6	71.5
25	0.971	35.3	29.4	29.4
50	0.990	36.0	28.0	14.0
100	0.993	36.1	27.9	7.0

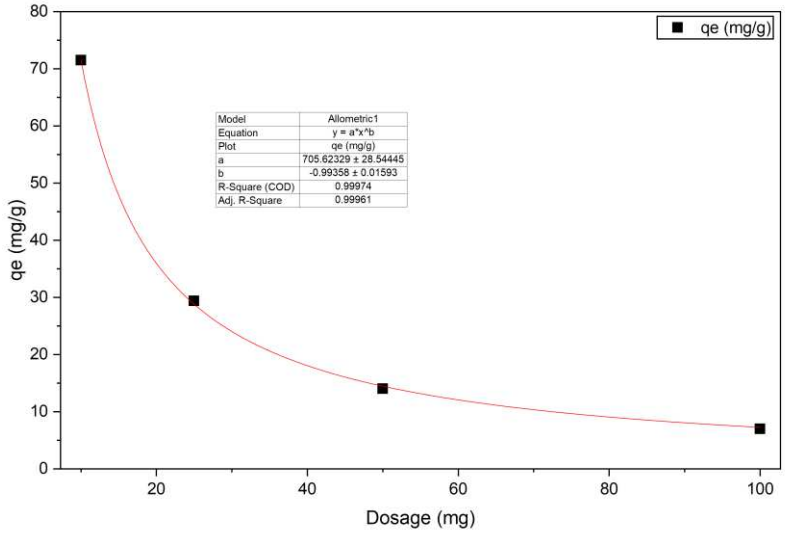


Figure 14. Effect of adsorbent dosage on removal efficiency and adsorption capacity.

Percentage removal remained relatively constant (27.9−29.4%) across the dosage range tested, with the highest value observed at 25 mg, while adsorption capacity decreased sharply from 71.5 mg/g at 10 mg to 7.0 mg/g at 100 mg. This is attributable to the fixed pool of cefuroxime molecules being distributed across an increasing mass of adsorbent, reducing the effective quantity adsorbed per unit mass, as well as to potential particle aggregation at higher adsorbent loadings, which would reduce the surface area available per unit mass. A dosage of 25 mg was therefore selected as optimum, balancing removal efficiency against adsorbent material use.

Effect of Temperature and Thermodynamic Parameters. The effect of temperature was investigated at pH 2 (25 mg adsorbent, 50 mg/L cefuroxime, 120 min contact time) over 25, 35, and 45 °C; results are presented in Table 11 and Figure 15.

Table 11. Effect of Temperature on Cefuroxime Adsorption

temp (°C)	temp (K)	Absorbance	Ce (mg/L)	removal (%)	qe (mg/g)
25	298	0.825	30.0	40.0	40.0
35	308	0.801	29.1	41.8	41.8
45	318	0.778	28.3	43.4	43.4

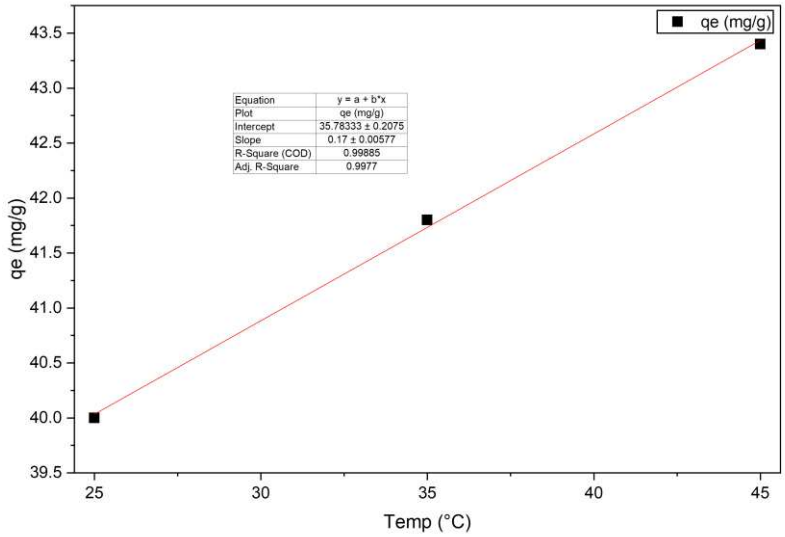


Figure 15. Effect of temperature on adsorption capacity.

Adsorption capacity increased modestly with temperature, from 40.0 mg/g at 25 °C to 43.4 mg/g at 45 °C. Thermodynamic parameters, derived from a van't Hoff plot of ln Kd against 1/T (Figure 16), are summarized in Table 12.

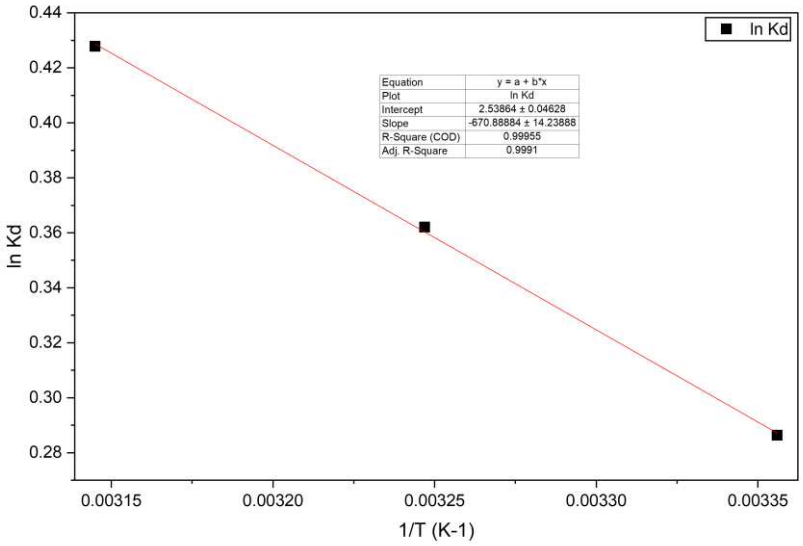


Figure 16. van't Hoff plot (ln Kd vs 1/T) for cefuroxime adsorption.

Table 12. Thermodynamic Parameters for Cefuroxime Adsorption

temp (K)	Kd	ΔG° (kJ/mol)	ΔH° (kJ/mol)	ΔS° (J/mol·K)
298	1.33	−0.71		
308	1.44	−0.92	+7.8	+28.2
318	1.53	−1.12		

The positive value of ΔH° (+7.8 kJ/mol) confirms that the adsorption process is endothermic, consistent with the observed increase in qe with rising temperature, while the positive ΔS° (+28.2 J/mol·K) suggests increased randomness at the solid−liquid interface during adsorption potentially reflecting the release of previously adsorbed water molecules from the adsorbent surface as cefuroxime molecules are adsorbed, together with some structural rearrangement of the phytochemical capping layer. The negative ΔG° values obtained at all three temperatures confirm that the adsorption process is spontaneous, with spontaneity increasing (ΔG° becoming more negative) as temperature rises, in agreement with the endothermic nature of the process.

CONCLUSION

Magnetite nanoparticles were synthesized using Ocimum gratissimum leaf extract via a green co-precipitation route, demonstrating the feasibility of this locally available plant as a green reducing and capping agent. UV-vis, FTIR, XRD, and SEM-EDX characterization confirmed the formation of a magnetite-dominant (55.6 wt %), phytochemical-capped, nanocrystalline iron oxide material with minor coexisting hematite, quartz, and clinochlore phases and an irregular, agglomerated morphology, consistent with an uncalcined, room-temperature green-synthesis route; this characterization profile offers a plausible explanation for the modest adsorption capacity obtained and highlights improved crystallinity and reduced agglomeration as directions for enhancing performance in future work.

The synthesized nanoparticles were effective in adsorbing cefuroxime from aqueous solution, with removal favored under acidic conditions (optimum pH 2) and equilibrium attained within 120 min. The adsorption process was best described by pseudo-second-order kinetics and the Langmuir isotherm model (qm = 62.5 mg/g), and was characterized as spontaneous and endothermic (ΔH° = +7.8 kJ/mol, ΔS° = +28.2 J/mol·K), with an adsorbent dosage of 25 mg giving the highest removal efficiency (29.4%). These findings provide empirical data on the adsorption kinetics, isotherms, and thermodynamics of cefuroxime removal by a plant-mediated nano adsorbent and support the development of an eco-friendly, low-cost route to pharmaceutical-pollutant remediation from water. Future work should explore post-synthesis calcination or surface functionalization to improve crystallinity and reduce agglomeration, adsorbent reusability and regeneration, continuous-flow column studies, complementary characterization by TEM, VSM, and XPS, and toxicity and biocompatibility assessment before field-scale application.

EXPERIMENTAL METHODS

Materials. All chemicals used in this study were of analytical grade and were used without further purification, including iron (III) chloride hexahydrate ($FeCl_3 \cdot 6H_2O$), iron (II) sulfate heptahydrate ($FeSO_4 \cdot 7H_2O$), sodium hydroxide (NaOH), hydrochloric acid (HCl), cefuroxime sodium ($C_{16}H_{16}N_4Na_8S$), ethanol (C_2H_5OH), and distilled water. Equipment used included an analytical balance, a magnetic stirrer with hot plate, a pH meter, an oven, a centrifuge, a UV-vis spectrophotometer, an FTIR spectrometer, an X-ray diffractometer, a scanning electron microscope, an orbital shaker, and a permanent neodymium magnet for nanoparticle separation. Fresh, healthy, disease-free leaves of *Ocimum gratissimum* were collected from Kaduna State, Nigeria, and authenticated by a botanist, with a voucher specimen deposited.

Preparation of *Ocimum Gratissimum* Leaf Extract. Fresh leaves were washed, air-dried for 7−10 days, ground to a fine powder, and sieved (0.5 mm). Twenty grams of the powder was added to 200 mL of distilled water, heated at 60 °C for 30 min with stirring, cooled, and filtered through Whatman No. 1 filter paper. The filtrate was stored at 4 °C before use[13].

Green Synthesis of Magnetite Nanoparticles. An iron-salt solution was prepared by dissolving $FeCl_3 \cdot 6H_2O$ (0.02 mol) and $FeSO_4 \cdot 7H_2O$ (0.01 mol) in 100 mL of distilled water. The solution was heated to 70 °C with stirring, and 50 mL of the leaf extract was added dropwise. The pH was adjusted to 9−10 with 1 M NaOH, and the mixture was stirred at 70 °C for 60 min. The resulting magnetite nanoparticles were separated using a permanent neodymium magnet placed against the wall of the reaction vessel, allowing the supernatant to be decanted; a ferrite magnet may be used as a lower-cost alternative. The collected nanoparticles were washed several times with distilled water and ethanol to remove unbound phytochemicals and impurities, dried in an oven at 60 °C for 12 h, and ground to a fine powder[18–20]. Extract concentration (5−25% v/v), pH (7−11), temperature (50−90 °C), reaction time (30−90 min), and iron-salt concentration (0.05−0.4 M) were varied to determine the optimal synthesis conditions. A schematic of the overall methodology is presented in Figure 17.

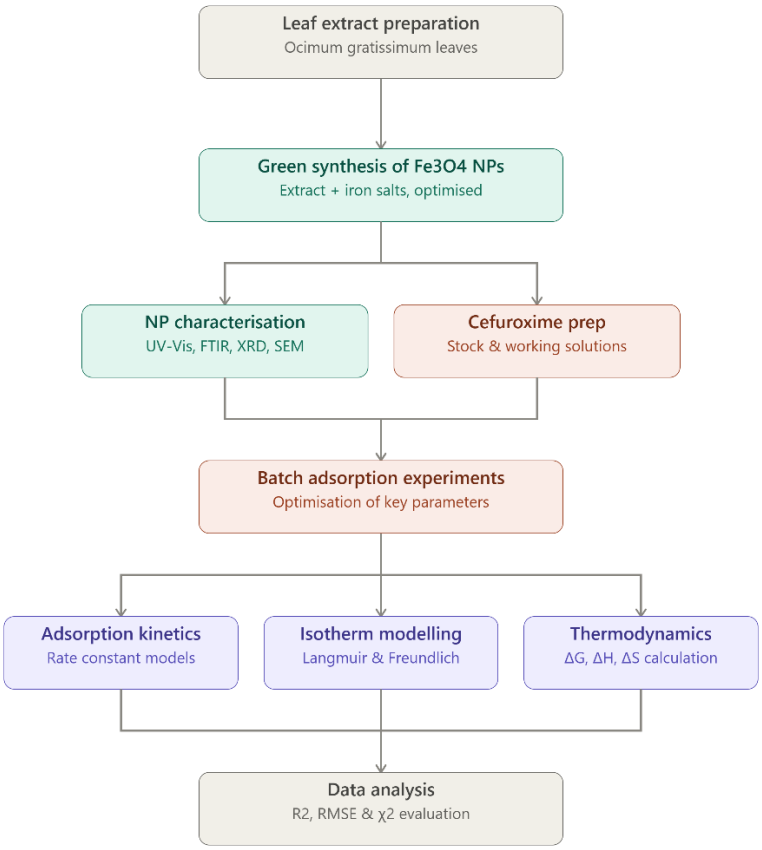


Figure 17. Flow chart of the experimental methodology.

Characterization of Nanoparticles. The synthesized nanoparticles were characterized as follows. UV-vis spectrophotometry: nanoparticles dispersed in distilled water were scanned over 200−800 nm to confirm nanoparticle formation[13,18]. FTIR spectroscopy: dried nanoparticles mixed with KBr (1:100) were pressed into pellets and scanned over 4000−400 cm^{-1} to identify surface functional groups[13,18,21]. XRD analysis: samples were scanned over 2θ = 20−80° using Cu Kα radiation, and crystallite size was estimated using the Debye−Scherrer equation:

$$D = K\lambda/(\beta \cos \theta)$$

where D is the crystallite size, K is the shape factor, λ is the X-ray wavelength, β is the full width at half-maximum of the diffraction peak, and θ is the diffraction angle[13,18]. SEM analysis: gold-coated nanoparticles were examined at various magnifications to assess morphology and size distribution[18,20].

Batch Adsorption Experiments. A stock cefuroxime solution (1000 mg/L) was prepared by dissolving 100 mg of cefuroxime in 100 mL of distilled water, and working solutions (10−100

mg/L) were prepared by dilution; concentrations were determined by UV-vis spectrophotometry at the wavelength of maximum absorption (λmax). In the general adsorption procedure, 25 mg of nanoparticles was added to 50 mL of cefuroxime solution in a conical flask and agitated at 150 rpm; the nanoparticles were then separated using a magnet, and the residual concentration was determined by UV-vis spectrophotometry. All experiments were carried out in triplicate. Adsorption capacity (qe) and percentage removal (%R) were calculated as:

$$qe = (C0 - Ce)\, V/m \qquad \%R = [(C0 - Ce)/C0] \times 100$$

where C0 and Ce are the initial and equilibrium cefuroxime concentrations (mg/L), V is the solution volume (L), and m is the adsorbent mass (g)[1,5]. The effect of solution pH was investigated over pH 2−10 (50 mg/L cefuroxime, 25 mg adsorbent, 120 min contact time); the effect of contact time was investigated over 5−180 min at the optimum pH; the effect of initial concentration was investigated over 10−100 mg/L at the optimum pH and equilibrium time; the effect of adsorbent dosage was investigated over 10−100 mg at the optimum pH and equilibrium time (50 mg/L cefuroxime); and the effect of temperature was investigated at 25, 35, and 45 °C for the thermodynamic studies.

Adsorption Kinetics, Isotherms, and Thermodynamics. Adsorption kinetics were evaluated using the pseudo-first-order, pseudo-second-order, and intraparticle diffusion models:

$$\log (qe - qt) = \log qe - (k1/2.303)\, t$$

$$t/qt = 1/(k2qe2) + (1/qe)\, t$$

$$qt = kidt1/2 + C$$

Equilibrium data were fitted to the Langmuir and Freundlich isotherm models:

$$Ce/qe = 1/(qmKL) + Ce/qm$$

$$\log qe = \log KF + (1/n) \log Ce$$

Thermodynamic parameters were determined from the distribution coefficient (Kd = qe/Ce), the Gibbs free energy relation (ΔG° = −RT ln Kd), and the van't Hoff equation:

$$\ln Kd = \Delta S°/R - \Delta H°/RT$$

with ΔH° and ΔS° obtained from the slope and intercept, respectively, of a plot of ln Kd against 1/T[1,5,10,22].

Data Analysis. Results are expressed as mean ± standard deviation of triplicate measurements. Statistical analysis was performed using Microsoft Excel and OriginPro 2021, and the goodness of model fit was evaluated using the coefficient of determination (R^2), root mean square error (RMSE), and chi-square (χ^2) tests.

AUTHOR INFORMATION

Corresponding Author

Shaaban Sallau − Department of Chemistry, Faculty of Science, Air Force Institute of Technology, Kaduna, Nigeria; Email: sallaushaaban@gmail.com

Author Contributions

J. A. wrote the manuscript, while S.S. and JYI supervised, reviewed, and edited the Manuscript

Funding

The authors did not receive funding from any organization for this research.

Declarations

Ethics approval and consent to participate

The plant was cultivated, not wild, and no local or national guidelines were followed in the collection of these plant parts in Nigeria. As such, no permission or licence was obtained, as we don't have such in Nigeria.

Consent for publication

All authors have duly reviewed the manuscript and thereby consent to its publication.

Competing interests

The authors declare no competing interests.

Data availability

All data generated or analysed during this study are included in this published article.

ACKNOWLEDGMENTS

The authors thank the Department of Chemistry, Air Force Institute of Technology, Kaduna, for providing the facilities and support that made this work possible.

REFERENCES

(1) Ren, X.; Li, Y.; Feng, T.; Lei, J.; Cheng, L. Removal of Cefuroxime from Aqueous Solution by Biochars Derived from Antibiotic Mycelial Residue. Environ. Sci. Pollut. Res. 2024, 31 (51), 61049−61059.

(2) Wroński, M.; Trawiński, J.; Skibiński, R. Electrochemical Removal of Cephalosporin Antibiotic-Cefuroxime Axetil from Aquatic Media Using Boron-Doped Diamond Electrodes: Process Optimization, Degradation Studies and Transformation Products Characterization. Molecules 2025, 31 (1), 106.

(3) Zeghbib, S.; Nasrallah, N.; Hafsa, H.; Kebir, M.; Tahraoui, H.; Lekmine, S.; Zeghbib, W.; Amrane, A.; Ahmed Ali, F. A.; Fadhillah, F.; Assadi, A. A. Solar-Driven Photocatalytic Removal of Cefuroxime

from Water: Process Optimization via Machine Learning and Nature-Inspired Algorithms. RSC Adv. 2025, 15 (38), 31767−31787.

(4) Ngwu, C. M.; Nnaji, J. C.; Odoemelam, S. O.; Amaku, F. J. Comparative Studies on the Chemo- and Biosynthesized Nanomaterials for the Remediation of Pharmaceutical Residues in Wastewater. J. Chem. Soc. Niger. 2020, 45 (6).

(5) Babarinde, I. M.; Adeyi, A. A.; Popoola, L. T.; Olateju, I. I.; Giwa, A. Novel Blighia sapida Leaf-Derived Biochar (BSLB) for Highly Efficient Removal of Cefuroxime from Aqueous Media. Adv. Mater. Res. 2025, 1185, 61−74.

(6) Shah, S. I. A.; Ahmad, W.; Anwar, M.; Shah, R.; Khan, J. A.; Shah, N. S.; Al-Anazi, A.; Han, C. Synthesis, Properties, and Applications of Fe_3O_4 and Fe_3O_4-Based Nanocomposites: A Review. Appl. Catal. O: Open 2025, 203, 207049.

(7) Das, C.; Biswas, G. Magnetically Driven, Plant-Extract-Modified Fe_3O_4 Nanoparticles for Sustainable and Eco-Friendly Wastewater Detoxification: Recent Developments. Nanoscale Adv. 2026, 8 (3), 743−781.

(8) Zhou, J.; Liu, J.; Liu, Y.; Wu, X.; Fujii, M. Boosted Antibiotic Degradation Using Magnetite Nanoparticles Doped Ultrafine Activated Charcoal Powder to Activate H2O2: Insights into Mechanisms and Competitive Kinetics. Environ. Res. 2025, 268, 120769.

(9) Sharma, M.; Sharma, K.; Kumar, D.; Gill, F. S.; Ichikawa, T.; Jain, A.; Shrivastava, K. Process Analysis of Aqueous Ciprofloxacin Adsorption by Biochar-Magnetite Nanocomposites. Discov. Appl. Sci. 2025, 7 (10), 1216.

(10) Yang, Y.; Zhu, Y.; Chen, J.; Zhou, X.; Zhang, Y. The Role of Ligand in the Activation of Peroxymonosulfate by Fe_3O_4 for the Degradation of Organic Pollutants. Sep. Purif. Technol. 2024, 338, 126543.

(11) Gwada, C. A.; Ndivhuwo, P. S.; Matshetshe, K.; Aradi, E.; Mdluli, P.; Moloto, N.; Otieno, F.; Airo, M. Phytochemical-Assisted Synthesis, Optimization, and Characterization of Silver Nanoparticles for Antimicrobial Activity. RSC Adv. 2025, 15 (18), 14170−14181.

(12) Nayak, S.; Goveas, L. C.; Mutalik, S.; Sajankila, S. P. Onsite Detection of Cadmium and Nickel Using Gold Nanospheres and Nanotriangles Capped with Cyclea peltata Phytochemicals. Environ. Nanotechnol. Monit. Manage. 2023, 20, 100815.

(13) Abdi, M.; Yusuf, Z.; Sasikumar, J. M. Phyto-Fabrication of Cobalt Oxide Nanoparticles from Ocimum gratissimum L. Leaf and Flower Extracts and Their Antimicrobial Activities. Open Biotechnol. J. 2023, 17 (1), e18740707261876.

(14) Alex, A. M.; Subbaraman, S.; Chauhan, S.; Ahuja, V.; Abdi, G.; Tarighat, M. A. Green Synthesis of Silver Nanoparticle Prepared with Ocimum Species and Assessment of Anticancer Potential. Sci. Rep. 2024, 14 (1), 11707.

(15) Ibrahim, A.; Ado, A.; Gabi, B.; Abdul-Azeez, U. M.; Bako, A. U.; Babagana, M. Phytogenic Synthesis, Structural Elucidation and Antiplasmodial Activity of Ocimum Gratissimum-Mediated Silver Nanoparticles Against Plasmodium Falciparum Clinical Isolate. UMYU Sci. 2025, 4 (3), 427−436.

(16) Nzerema, C. M.; Nna, P. J.; Orie, K. J. Synthesis and Characterization of Silver Nanoparticles Using Ocimum gratissimum Root Extract and Their Biological Activities Against Some Clinical Pathogens. Acta Chim. Asiana 2025, 8 (2), 672−681.

(17) Ogunleye, G. E.; Oyinlola, K. A.; Akintade, O.; Fashogbon, R.; Adesina, T. Green Synthesis, Characterization and Antimicrobial Potential of Selenium Nanoparticles from Ocimum gratissimum. Turk. J. Agric. Food Sci. Technol. 2022, 10 (sp2), 2903−2912.

(18) Begum, S. K.; Shabnam, D.; Haque, N.; Alam, M. J.; Ferdous, J.; Nur, U. J. B.; Fatema, K.; Shabiha, R. J.; Clarke, R. J.; Chowdhury, P.; Uddin, Md. N. Green Synthesis of Magnetite (Fe_3O_4) and Hematite (Fe_2O_3) Nanoparticles Using Moringa oleifera and Psidium guajava Leaf Extracts for Sustainable Applications. Sci. Rep. 2025, 15 (1), 36465.

(19) Khelali, A.; Benmahdi, F.; Sahnoune, D.; Sami, K.; Hacıosmanoğlu, G. G.; Akram, S.; Isinkaralar, K.; Siswanta, D.; Hosseini-Bandegharaei, A. Removal of AG 25 Dye from Aqueous Solutions and Treatment of Real Tannery Wastewater by Reusable Magnetic Iron Oxide Nanoparticles Loaded with Pomegranate Pomace Extract. Environ. Res. 2025, 279, 121744.

(20) Laxmi Mangamma, J.; Basavaiah, K. Facile Green Fabrication of Magnetite Nanoparticles Using an Aqueous Flower Extract of Murraya paniculata (L) Jack for an Efficient Removal of Organic Dye Pollutant, Antibacterial Activities. Inorg. Chem. Commun. 2024, 162, 112290.

(21) Saaduldeen Anwer, S. Simultaneous Green Synthesis of Magnetite-Nanoparticles MNPs Using Microalgae Spirulina sp. for Antibacterial Activity. Emir. J. Food Agric. 2023.

(22) Ma, D.; Cheng, Z.; Yuan, Y.; Chaem Chuen, S. Activation of 2D/3D Zeolitic-Imidazole Frameworks Affecting Crystal Properties and Adsorption Performance. J. Environ. Chem. Eng. 2024, 12 (3), 112845.